

Thermal conductivity of Si nanowires: A first-principles analysis of the role of defects

By. Kang and S. K. Estreicher

Physics Department, Texas Tech University, Lubbock, Texas 79409-1051, USA

(Received 11 December 2013; revised manuscript received 24 January 2014; published 7 April 2014)

The theoretical laser-flash method is used to calculate the thermal conductivity of the $\text{Si}_{200}\text{X}_{32}$ ($X = \text{H}, \text{D}, \text{or OH}$) and $\text{Si}_{296}\text{X}_{112}$ ($X = \text{H or D}$) nanowires. The main emphasis is on the role of defects, which are described using first-principles methods. The defects considered are the surface of the nanowire, random distributions of substitutional C or Ge impurities, and monoatomic δ layers of C or Ge. The localized vibrational modes of these defects are explicitly included in the calculations and no empirical defect-related parameter is introduced. We find that the surface Si–H wag modes couple resonantly to each other much faster than they decay into bulk modes, which leads to distinct surface and bulk contributions to the thermal conductivity. The spatially-localized vibrational modes associated with the Ge or C impurities as well as the δ layers trap thermal phonons thus reducing the thermal conductivity.

DOI: [10.1103/PhysRevB.89.155409](https://doi.org/10.1103/PhysRevB.89.155409)

PACS number(s): 61.72.S–, 63.20.dk

I. INTRODUCTION

It is well known [1,2] that the presence of defects reduces the phonon contribution to the thermal conductivity of materials. Since the pioneering work of Peierls in the 1920s, this reduction has been described in terms of the scattering of (bulk) phonons by static defects. This empirical description has been refined over the years by several authors [3–5]. Today, the concept of phonon scattering by a wide range of defects (impurities, interfaces, boundaries, surfaces, etc.) is the commonly accepted way to include defects in the calculation of thermal conductivities (see, e.g., Refs. [6–10]).

But defects are dynamic. Light impurities introduce local vibrational modes (LVMs). They are high-frequency vibrational modes that give rise to infrared absorption or Raman spectra [11]. Photoluminescence spectra of transition-metal impurities in Si often show phonon sidebands characteristic of low-frequency impurity-related pseudolocal modes [12,13] implying that impurities also give rise to low-frequency localized vibrational modes.

In a recent paper [14], we have shown that *spatially localized modes* (SLMs) are associated with all types of defects. These normal vibrational modes involve oscillations of only a few atoms at (near) the defect. These modes are localized in space, and LVMs are just a special type of high-frequency SLMs. The localization of such modes can be quantified using the eigenvectors of the dynamical matrix. Strongly localized SLMs are associated with isolated impurities, native defects, interfaces, surfaces, heterojunctions, and other defect structures. Some low-frequency modes sometimes exhibit surprisingly large spatial localization [14].

A SLM can trap a phonon following an optical (high-frequency modes) or thermal (low-frequency modes) excitation. The energy $\hbar\omega$ remains localized at the defect for a length of time called the vibrational lifetime. Thus defects in semiconductors not only trap electric charge (e^- or h^+) but also energy, a phenomenon called phonon trapping [15]. Vibrational lifetimes vary from a few ps to a few hundred ps depending on the defect and sometimes its isotopic composition [16–18].

When bulk phonons carrying heat through a material encounter a defect, they excite SLMs which trap phonons. After

some time, the excitations decay into combinations of bulk phonons different from the ones that generated the excitation. The net result is that the interaction of bulk phonons with defects does indeed generate new bulk phonons. The shortcut for this series of events is called “phonon scattering” but this ignores phonon trapping, the nature of the SLMs, and—more importantly perhaps—the vibrational lifetimes involved. Indeed, the word scattering implies a quasi-instantaneous event, while the lifetimes of the SLMs correspond to dozens or hundreds of periods of oscillation [14]. The memory of where the excitation originally came from is lost and the process is more subtle than the word scattering implies.

The focus of this paper is on an atomistic description of the role of defects on the thermal conductivity of Si nanowires. We use nonequilibrium *ab initio* molecular-dynamics (MD) simulations in 1-D periodic supercells prepared slightly away from thermal equilibrium. The defects considered here are the surface of the nanowire, a monoatomic δ layer of C or Ge atoms, and a random distribution of C or Ge substitutional impurities. The impact of the defects is not described using empirical “defect scattering” parameters. Instead, all the normal vibrational modes of the system, including the SLMs associated with the defects, are explicitly included.

The thermal conductivities of Si nanowires have been calculated by several groups, using the accepted “phonon scattering” picture to describe defects. Some of these calculations involved solving the Boltzmann transport equation and phonon dispersion relations [10,19–21]. The (bulk) phonon lifetimes are obtained from Matthiessen’s rule, expressing the inverse total lifetime as the sum of inverse lifetimes associated with each scattering mechanism (such as normal, Umklapp, impurity, surface, or defect scattering). These calculations involved nanowires with much larger diameters than the ones we are able to consider using our first-principles approach.

Other authors used nonequilibrium MD simulations. A temperature gradient was maintained with the use of a thermostat until a steady-state configuration was achieved [22,23]. The electronic problem was solved using the Stillinger-Weber empirical potential. Such methods are powerful when dealing with defect-free systems, but empirical potentials are not easily transferable to situations where defects or impurities are present [24].

Section II describes the supercells and the theoretical laser-flash approach. Section III focuses on the dynamics of defects (surface, δ layers, and random distribution of impurities) and their impact on the thermal conductivity. The key results are discussed in Sec. IV.

II. METHODOLOGY

The theoretical laser-flash method [25,26] begins with the preparation of supercells in (or slightly away from) thermal equilibrium at moderate temperatures using the eigenvalues and eigenvectors of the dynamical matrix. No thermalization run is needed and no thermostat is used during the subsequent MD simulations. The temperature fluctuations are very small, especially after averaging over a range of initial normal-mode phases and energies. Temperature increases of 10 K (from 115 to 125 K) can easily be monitored. Even smaller temperature changes can be obtained in 3D-periodic supercells, which are not as elongated as the 1D ones used here. The electronic structure calculations are done within density-functional theory (DFT).

A. Supercells

Two supercells were used in this study (Fig. 1): $\text{Si}_{200}\text{X}_{32}$ with $X = \text{H}, \text{D}, \text{or OH}$ groups, and $\text{Si}_{296}\text{X}_{112}$ with $X = \text{H}$ or D . Periodic boundary conditions are applied only in the x direction. The supercells are constructed from truncated slices of crystalline Si aligned along the $\langle 100 \rangle$ direction and the surface dangling bonds are terminated with H, D, or OH groups. Although the H termination of Si nanowires can in principle be achieved, e.g., with a brief HF dip, Si nanowires

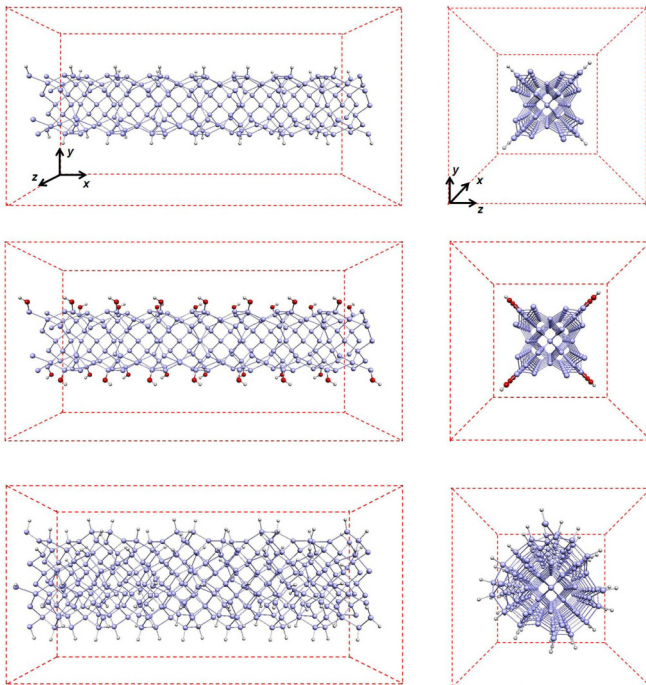


FIG. 1. (Color online) Side and cross-section view of the three Si nanowires used in the present study. The Si atoms are light blue, the surface H (or D) atoms are white, and the O atoms are red.

exposed to air have a thin surface oxide, the atomistic nature of which is not known. As discussed below, the OH termination is not particularly stable.

The $\text{Si}_{200}\text{H}_{32}$ [or $\text{Si}_{200}(\text{OH})_{32}$] supercell can be described as eight alternating “slices” Si_{13}H_2 and Si_{12}H_2 [or $\text{Si}_{13}(\text{OH})_2$ and $\text{Si}_{12}(\text{OH})_2$] appended along the $\langle 100 \rangle$ direction. The $\text{Si}_{296}\text{H}_{112}$ supercell consists of four alternating slices Si_{25}H_6 and $\text{Si}_{49}\text{H}_{22}$. The diameters of these nanowires are 13.18, 14.67, and 14.70 Å, respectively (including the surface atoms). The sides (along the y and z directions) of the square box containing the nanowires must be equal or greater than 22, 22, and 26 Å, respectively, in order to contain the optimized orbitals (Sec. II C). Along the x direction, the optimized length of the box is almost the same for these three nanowires, 43.18, 43.18, and 41.53 Å, respectively. As mentioned earlier, our study focuses on the role of defects (for which first-principle theoretical techniques must be used) and not on size effects (which are best handled using semiempirical methods, as much larger numbers of atoms can be calculated).

B. Geometry optimizations

In order to obtain accurate dynamical matrices (no negative eigenvalues), the geometries must be carefully optimized. In 3D periodic supercells, this is done in two steps. First, the lattice constant(s) of the defect-free cell is (are) optimized in each charge state, for each basis set, and for each exchange-correlation potential. This is best done with nuclear coordinates expressed in units of the lattice constant: nuclear coordinates such as (0.25, 0.25, 0.25) are exact and the lattice constant can be optimized up to many significant figures. This optimization of the dimensions of the box containing the atoms is easily carried out until the maximum force component is of the order of 10^{-6} eV/Å or less. Then, the defect is introduced and its geometry is optimized (in a box of fixed dimensions) using a conjugate-gradient algorithm until the maximum force component is smaller than 0.003 eV/Å.

The present situation is more complicated. The presence of surface atoms makes it impractical to write the nuclear coordinates in units of the lattice constants, as changing them affects not just the Si-Si bond lengths but also the surface Si-H bond lengths and angles. Along the y and z directions, the dimensions of the box must be greater than the extent of the orbitals of the surface atoms in order to simulate a vacuum region. However, along the x direction, the geometry of the nanowire is difficult to optimize to the needed level of accuracy because the geometries of the Si and surface atoms are highly sensitive to very small changes of the lattice constant. Our most careful optimizations of the lattice constants produce dynamical matrices with a few unwanted negative eigenvalues. We had to displace the atoms by hand along the eigenvectors of the dynamical matrix associated with each negative eigenvalue until the absolute minimum of the potential energy surface was reached and no negative eigenvalues occurred.

When a δ layer was introduced into the system, simple conjugate gradient calculations produced excellent dynamical matrices. When a random distribution of Ge substitutional impurities was introduced, a simple conjugate gradient calculation achieved the desired geometry optimization, because substitutional Ge is a very small perturbation in Si. However,

substitutional C impurities produce a substantial change in the crystal (large inward displacement of the four Si neighbors to C). In this case, we had to perform conjugate gradient optimizations for each substitutional C successively introduced into the nanowire. In the end, none of the calculated dynamical matrices had negative eigenvalues.

C. Electronic structure

The core regions are removed from the calculations using *ab initio*-type norm-conserving pseudopotentials with the Troullier-Martins parametrization [27] in the Kleinman-Bylander form [28]. The valence regions are described within DFT with the exchange-correlation potential of Ceperley and Alder [29] as parameterized by Perdew and Zunger [30]. We use the SIESTA [31,32] method.

The basis set for the valence states are numerical pseudoatomic orbitals of the Sankey type [33,34]. We use a double- ζ basis set for H, C, and O (two sets of s and p orbitals), and add polarization functions (a set of d 's) to Si and Ge. Each orbital is truncated beyond a cutoff radius r_c and then renormalized. In general, larger r_c 's provide better quality orbitals (i.e., lower energies), but also increase the computational effort because the overlap matrix contains more nonzero elements. In this work, the r_c 's for the orbitals of nonsurface atoms are those optimized by Anglada *et al.* [35]. For bulk Si atoms, they are of the order of $5a_B$. Thus Si atoms farther than $\sim 10a_B$ apart do not overlap. This works very well in 3D-periodic supercells as the total energy varies insignificantly for larger values of r_c .

However, surface atoms have no neighbor in the direction of free space, and their orbitals must be allowed to extend into the vacuum region of the box. For computational reasons, setting $r_c \rightarrow \infty$ is obviously impractical. A useful compromise was proposed by Garcia *et al.* [36]. It involves minimizing a fictitious enthalpy $H = E + PV$ for each orbital i , where $V_i = (4\pi/3)r_{ci}^3$. By varying the pressure parameter P , one

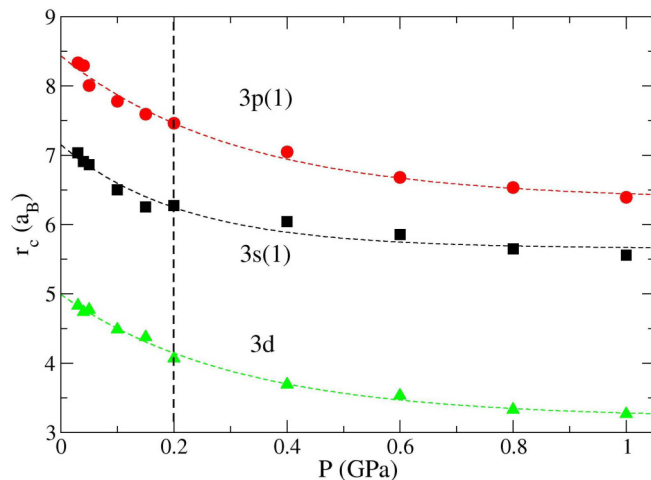


FIG. 2. (Color online) Calculated orbital radii r_c for the first- ζ ($3s$ and $3p$) and the $3d$ valence orbitals of the surface Si atoms. The second- ζ orbitals behave in a similar manner. The thin dashed lines are exponential fits. The thick vertical dashed line shows the fictitious pressure $P = 0.2$ (GPa) used in this work.

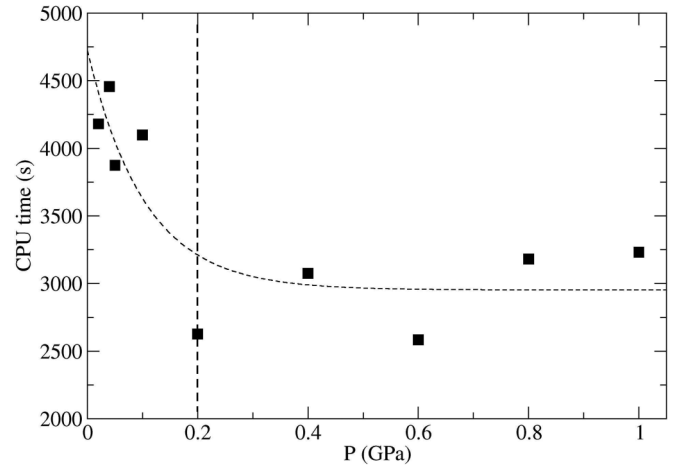


FIG. 3. Computer time vs the fictitious pressure parameter P . The thin dashed line is a simple exponential fit. Low values of P lead to large orbital radii r_c , overlap matrices with a larger number of nonzero elements, and longer CPU times.

can optimize r_c without going to the limit $r_c \rightarrow \infty$. Figure 2 show typical examples of the calculated r_c versus P for the double- ζ polarized basis set of Si. In the present calculations, the fictitious pressure $P = 0.2$ (GPa) was chosen. Figure 3 shows the computer time versus P .

D. Dynamical matrix and supercell preparation

The central ingredient of the theoretical laser-flash method is the dynamical matrix, calculated at $k = 0$. Its eigenvalues ω_s are the normal-mode frequencies of the system. Its orthonormal eigenvectors $e_{\alpha i}^s$ give the relative displacement of atom α along the direction $i = x, y, z$ for each normal mode s .

A quantitative measure of the spatial localization of mode s on one atom or a group of atoms is provided by a plot of $L^2\{\alpha\} = (e_{\alpha x}^s)^2 + (e_{\alpha y}^s)^2 + (e_{\alpha z}^s)^2$ versus ω_s . If $\{\alpha\}$ includes all the atoms in the system, the sum is of course equal to 1. If $\{\alpha\}$ includes a single atom (e.g., H) or a group of atoms (e.g., all the H atoms on the surface of the nanowire), then the sum is smaller than 1. In the case of a bulk mode, which involves the motion of many (or all) the atoms in the system, $L^2\{\alpha\}$ calculated for just one atom is a very small number. However, for a SLM, it can be quite large.

In addition to providing a quantitative measure of the spatial localization of normal modes, the eigenvectors of the dynamical matrix $e_{\alpha i}^s$ can be used to prepare (parts of) the supercell in thermal equilibrium at the temperature T . Indeed, the Cartesian coordinates $r_{\alpha i}^s$ are related to these eigenvectors $r_{\alpha i}^s(T, t) = q_s(T, t) e_{\alpha i}^s$, where $q_s(T, t)$ are the normal-mode coordinates.

The simplest way to prepare the supercell in thermal equilibrium at $t = 0$ is to assume that the modes are harmonic, that is $q_s(T, t) = A_s(T) \cos(\omega_s t + \varphi_s)$. This introduces a random distribution of phases φ_s for each mode. Note that the subsequent nonequilibrium MD simulations do not assume harmonicity at all since the atomic displacements are calculated using forces derived from total energies at every time step. The unknown amplitudes $A_s(T)$ are obtained by

requiring that, in thermal equilibrium, the *average* energy of each mode is $k_B T$. In our calculations [16,26], this requirement introduces the Maxwell-Boltzmann distribution $\zeta_s = \int_0^{E_s} (e^{-E/k_B T} / k_B T) dE$. Selecting a random value of ζ_s (in the range $[0, 1]$) and φ_s (in the range $[0, 2\pi]$) determines the distribution of mode energies and phases and thus the position and velocity of all the atoms in the supercell at the time $t = 0$ approximating (quite well) thermal equilibrium at the temperature T .

E. Nonequilibrium MD

The nuclei obey classical laws of motion with forces obtained from total energies via the Hellmann-Feynman theorem [37,38]. The Verlet algorithm is used to calculate the position and velocity of the nuclei at the time $t + \Delta t$, where the time step Δt is chosen to be a small fraction of the fastest oscillation period in the system. In our case, this would be the Si-H (or O-H) stretch mode, which has period of about 15 (or 10) fs, respectively. We used Δt in the range 0.2 to 1.0 fs. The temperature in each slice of the supercell is obtained from the kinetic energy of the nuclei.

MD simulations in supercells prepared slightly away from thermal equilibrium produce small temperature fluctuations starting with the first MD step. No thermostat can be used since it would artificially force the system back into thermal equilibrium much faster than the various vibrational modes actually couple. One must repeat the MD runs with many random distributions of initial mode phases and energies and then average the results. The averaging further reduces the temperature fluctuations (Fig. 4). In this study, we typically averaged the results over 100 runs, but tested individual results with up to 200 runs. Note that our microcanonical runs strictly conserve energy. The total temperature of the supercell

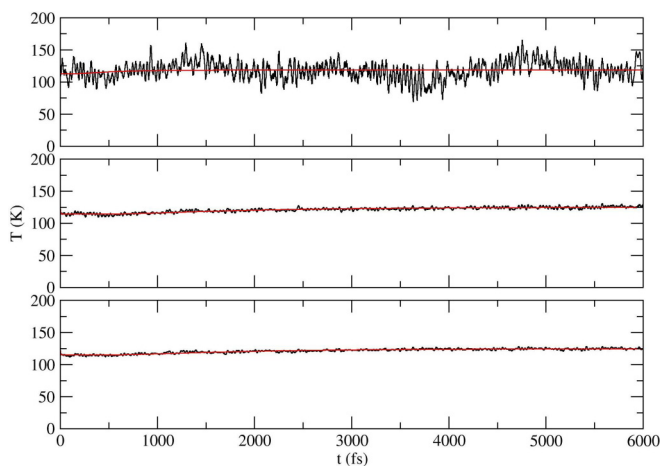


FIG. 4. (Color online) Temperature vs time in the central slice of the $\text{Si}_{200}\text{H}_{32}$ nanowire after a single run (top), and after averaging over 50 (middle) and 100 (bottom) runs. At the time $t = 0$, the first slice of the supercell was prepared $T_{\text{hot}} = 270$ K and the rest of the supercell at $T_{\text{cold}} = 115$ K. Thus the temperature in the central slice increased from $T_{\text{cold}} = 115$ K to $T_{\text{avg}} = 125$ K. No thermostat was used. The solid (red) line shows the fit to the analytic solution to the heat-diffusion equation (see text). Finer details of the temperature increase, not visible on this scale, are discussed in a further section.

remains constant for tens of thousands of time steps, be it for equilibrium or nonequilibrium, single or averaged runs.

F. Thermal conductivity

The evolution of the temperature $T(t)$ in the central slice can be used to obtain the thermal diffusivity α and then the thermal conductivity κ at the temperature T_{avg} . This is achieved by fitting the same analytic solution to the heat diffusion equation that is used in the experimental laser-flash method [39]:

$$T(t) = T_{\text{cold}} + (T_{\text{avg}} - T_{\text{cold}}) \sum_n (-1)^n \exp(-n^2 \pi^2 \alpha t / x^2),$$

where x is the distance between the hot slice and the central slice. The fit (Fig. 4) gives the thermal diffusivity α , and the thermal conductivity is given by $\kappa = \alpha \rho C$, where ρ is the density of the material and C is the specific heat calculated at T_{avg} using the phonon density of states of the system. Our sum runs up to $n = 10$.

Note that such nonequilibrium MD simulations and calculations of the thermal conductivity can be done with any electronic structure method provided that the geometries are optimized accurately (the dynamical matrix has no negative eigenvalues). Since we focus on the role of defects on the thermal conductivity, we use a first-principles electronic structure method. The computational cost (geometry optimizations, dynamical matrices, and especially averaging over many random distributions of initial mode phases and energies) can be substantial but the method is characterized by very small T fluctuations starting with the first MD step. This allows the use of much smaller temperature gradients than with conventional methods, and very small temperature changes in the central slice can be monitored (Fig. 2 in Ref. [25] and Fig. 2 in Ref. [26]).

III. THERMAL CONDUCTIVITY: THE ROLE OF DEFECTS

The theoretical laser-flash method is ideally suited to study the impact of defects on the thermal conductivity without reference to empirical phonon scattering parameters. All the normal vibrational modes are explicitly included in the calculations, the electronic structure is obtained from density-functional theory, and the nonequilibrium MD runs are performed at the *ab initio* level without thermostat and with excellent temperature control. On the other hand, the method is computationally demanding, especially because the results must be averaged over many runs, each with randomly generated initial mode phases and relative energies. Thus the method is not appropriate to calculate size effects related to the length or diameter of the nanowire.

However, we can compare the calculated thermal conductivities at a fixed temperature to an extrapolation of the experimental data [40] obtained at the same temperature in nanowires of various diameters (Fig. 5). Our values are consistent with the measured ones.

We can also compare our calculated $\kappa(T)$ to that measured in larger nanowires as a function of their diameter [40] (Fig. 6). The comparison is qualitative because our nanowire is perfectly H-terminated, while the experimental nanowires have some ill-defined oxide on the surface. However, the

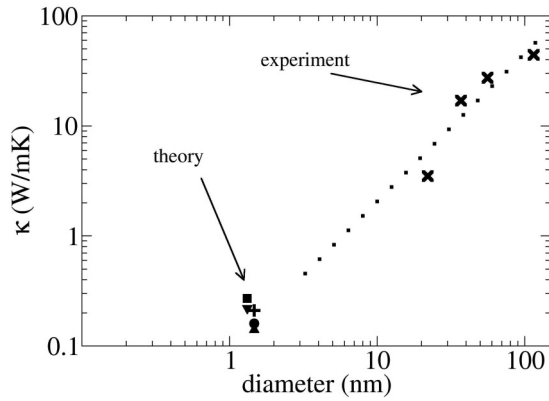


FIG. 5. The experimental thermal conductivities at $T = 125$ K (\times 's) have been obtained from Fig. 3 in Ref. [40]. The theoretical values are for nanowires with diameter (\AA) 13.18 ($\text{Si}_{200}\text{D}_{32}$, square), 13.18 ($\text{Si}_{200}\text{H}_{32}$, triangle down), 14.67 ($\text{Si}_{200}(\text{OH})_{32}$, cross), 14.70 ($\text{Si}_{296}\text{D}_{32}$, circle), and 14.70 ($\text{Si}_{296}\text{H}_{32}$, triangle up) diameter. The dotted line shows the extrapolation of the measured data to the size of our nanowires.

key features are well reproduced, such as the temperature at which κ is maximum, the drop in thermal conductivity with the diameter of the nanowire, and the general shape of the curve. These comparisons suggest that our calculated thermal conductivities are quite close to the experimental ones.

We consider next the role of the surface, and how it reduces the thermal conductivity. And then, we look at the impact of a monoatomic δ layer of Ge (heavier than Si) or C (lighter than Si), and compare it to the impact of the same impurities randomly distributed in the nanowire. The latter results are interpreted in terms of phonon trapping at the SLMs associated with the defects and their vibrational lifetimes. The spatial localization of vibrational modes, phonon trapping at defects, vibrational lifetimes, and decay channels are discussed in detail in Ref. [14].

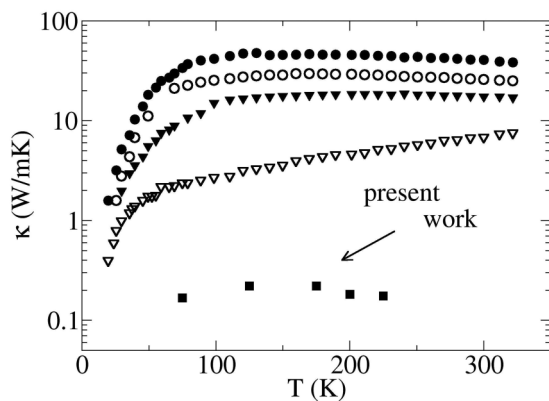


FIG. 6. Temperature dependence of the thermal conductivity calculated in $\text{Si}_{200}\text{H}_{32}$ (a diameter is 13.18 \AA , full squares) compared to the measured values in Si nanowires with diameter (top to bottom) 1150 (full circle), 560 (open circle), 370 (full triangles), and 220 \AA (open triangles) respectively (Fig. 3 in Ref. [40]). Note that the temperature at which $\kappa(T)$ is maximum and the general shape of the curve are generally consistent with the measured data.

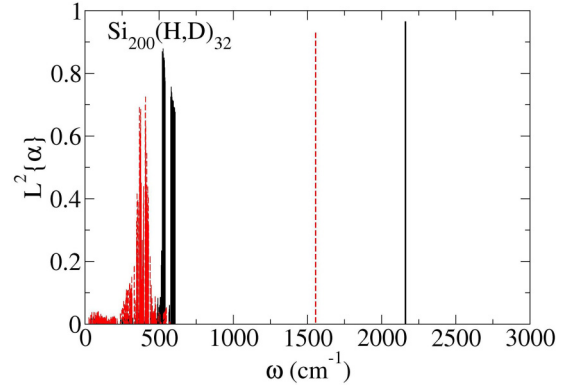


FIG. 7. (Color online) Spatial localization $L^2\{\alpha\}$ of the Si-H (black solid lines) and Si-D (red dashed lines) stretch and wag modes in $\text{Si}_{200}(\text{H,D})_{32}$. The highest-frequency Si-Si stretch mode in this nanowire is at 570 cm^{-1} , slightly higher than the optical phonon in crystalline Si.

A. Surface of the nanowire and resonant coupling

We used two Si nanowires with very different concentrations of H surface atoms. The ratio of surface-to-bulk atoms is $[\text{H}]/[\text{Si}] = 0.16$ for $\text{Si}_{200}\text{H}_{32}$ and 0.39 for $\text{Si}_{296}\text{H}_{112}$. The localization of the H- (or D-) related modes in the $\text{Si}_{200}\text{H}_{32}$ supercell is shown in Fig. 7. It consists of a narrow band of high-frequency Si-H (or Si-D) stretch modes and broader bands of Si-H (or Si-D) wag modes. All these modes are strongly localized on the surface of the nanowire.

As discussed in Ref. [14], all defects (impurities, grain boundaries, interfaces, surfaces, etc.) introduce SLMs into the vibrational spectrum. These modes can trap phonons and the vibrational energy remains trapped at the defect for lengths of time (the vibrational lifetimes) substantially longer than bulk vibrational modes of the same frequency. The phonons trapped in SLMs ultimately decay into lower-frequency modes. Thus defects always lower the thermal conductivity of the material by trapping heat in SLMs.

In the present case, the SLMs are the surface Si-H stretch and wag modes. The high-frequency stretch modes can only be excited optically, but the lower-frequency wag modes can be excited thermally in the hot slice of the supercell when the temperature gradient is applied.

We calculated the thermal conductivity of the $\text{Si}_{200}\text{H}_{32}$ and $\text{Si}_{296}\text{H}_{112}$ nanowires at 125 K. This was achieved by preparing the nanowire in thermal equilibrium at 115 K, raising the temperature of a thin slice (on the far left) to 270 K (for $\text{Si}_{200}\text{H}_{32}$) or 247 K (for $\text{Si}_{296}\text{H}_{112}$), and then monitoring the temperature increase in the central slice as a function of time. Once thermal equilibrium is reached, the temperature of the entire cell is 125 K. The results are shown in Fig. 8 for $\text{Si}_{296}\text{H}_{112}$, which has a surface-to-bulk ratio $[\text{H}]/[\text{Si}] = 0.39$. The figure shows that the central slice reaches thermal equilibrium in two steps. The first step corresponds to the heat carried by Si-related (bulk) phonons (increase in temperature $\Delta T_b \approx 5.9 \text{ K}$) and the second step to the heat propagating on the surface (increase in temperature $\Delta T_s \approx 3.1 \text{ K}$). Figure 9 shows the temperature of only the Si atoms and that of only the H atoms in the central slice.

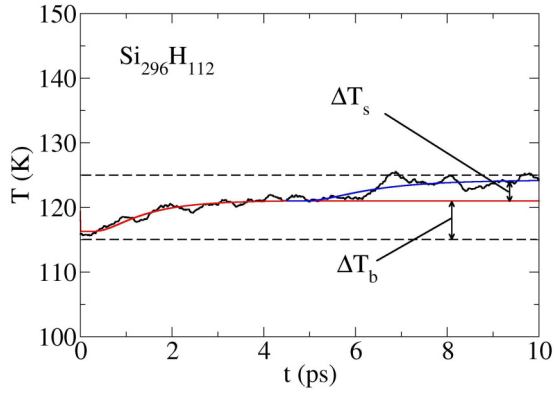


FIG. 8. (Color online) A thin slice of the $\text{Si}_{296}\text{H}_{112}$ supercell is prepared at 247 K and the temperature of the central slices is monitored at its temperature increases from 115 to 125 K. The temperature increases first when the bulk (Si-related) phonons reach the central slice, and later when the heat propagating along the surface arrives. The Si-H wag modes transport energy by resonant coupling, with a lifetime of the order of 0.5 ps at 125 K.

The same calculations performed in $\text{Si}_{200}\text{H}_{32}$ (which has a much smaller surface-to-bulk ratio, $[\text{H}]/[\text{Si}] \approx 0.19$) shows a comparatively smaller effect, with $\Delta T_b \approx 9.3$ K and $\Delta T_s \approx 1.5$ K, as shown in Fig. 10. A very similar process happens in D-terminated nanowires, even though the Si-D wag modes ($\sim 420 \text{ cm}^{-1}$) are within the phonon density of states of nanowire. Resonant coupling between adjacent Si-D wag modes occurs at somewhat faster than in the case of Si-H wag modes. Thus the heat trapped on the surface in the hot slice propagates along the surface by resonant coupling rather than decay into bulk modes. Surface and bulk modes do not mix.

The explanation for this behavior lies in the vibrational lifetime of the surface wag mode. Once such a mode is

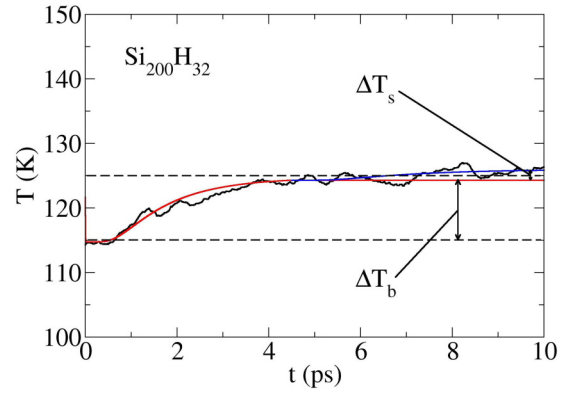


FIG. 10. (Color online) A thin slice of the $\text{Si}_{200}\text{H}_{32}$ supercell is prepared at 270 K and the temperature of the central slices is monitored at its temperature increases from 115 to 125 K. The temperature increases first when the “bulk” (Si-related) phonons reach the central slice, and later when the heat propagating along the surface arrives. The Si-H wag modes transport energy by resonant coupling, with a lifetime of the order of 1 ps at 125 K. The surface contribution is smaller than in the case of $\text{Si}_{296}\text{H}_{112}$ because of the smaller $[\text{H}]/[\text{Si}]$ ratio.

thermally excited in the hot slice of the supercell, the excitation can decay in two ways: it can resonantly couple to adjacent surface wag modes (of the same frequency) or decay into bulk phonons.

We have estimated the lifetime associated with the resonant coupling of Si-H wag modes as follows. The $\text{Si}_{200}\text{H}_{32}$ supercell was prepared at $T = 0$ K and one Si-H wag mode (583 cm^{-1}) was selected and given the initial amplitude $\sqrt{2k_b T / 2\pi\omega c}$, with $T = 400$ K. We then initiated a MD simulation and recorded the kinetic energy of this H atom as well as the kinetic energies of its H nearest and second-nearest neighbors. The first two ps of this run are shown in Fig. 11. Adjacent wag modes couple on a time scale of the order of 0.5ps, and the initial energy propagates back-and-forth among adjacent

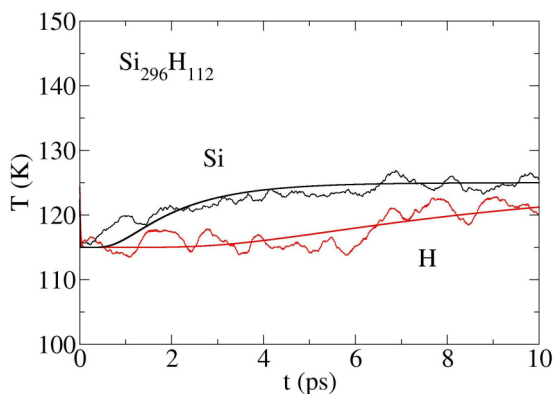


FIG. 9. (Color online) The temperature increases of only the Si atoms in the central slice compared to the temperature increase of only the H atoms in the same slice. The surface lowers the thermal conductivity because the heat propagates slower along the surface than in the bulk.

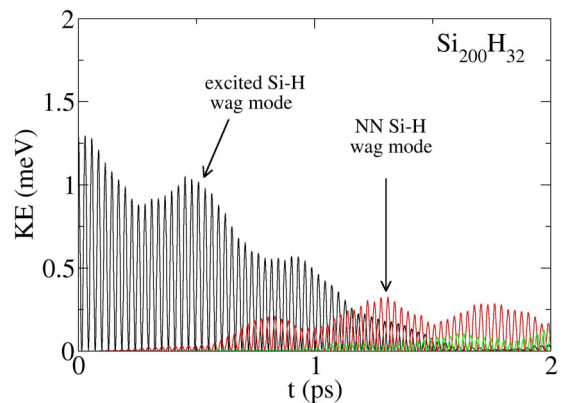


FIG. 11. (Color online) Kinetic energy (KE) of adjacent surface H atoms. One excited Si-H wag mode (black) couples resonantly to one of its nearest neighbor (NN, red) on a time scale shorter than 1 ps, consistent with the lifetime associate with the frequency-gap law [41]. The excitation of one second NN (green) can be seen in the color figure as well.

Si-H units. The coupling between adjacent Si-D wag modes is slightly shorter than for Si-H.

Resonant coupling is obviously a one-phonon process. The lifetime we estimate is consistent with the time scale of one-phonon processes predicted by the frequency-gap law [41]. This lifetime is still considerably longer than that associated with the excitation of bulk phonons [14].

The decay of the Si-H wag mode at 531 cm^{-1} (or Si-D at 368 cm^{-1}) wag mode into bulk phonons can be calculated using the techniques discussed in Refs. [16–18]. At 125 K, this decay is of the order of 15 to 20 ps for Si-H and slightly less than 10 ps for Si-D [42]. According the frequency-gap law [41], the former decay is at the upper end of a two-phonon decay or at the lower end of a three-phonon decay, while the latter corresponds to a two-phonon decay.

For temperatures below $\sim 500\text{ K}$, no Si-related mode has enough energy to excite a surface Si-H wag mode. Thus bulk modes do not couple with surface modes. As long as the surface is out of equilibrium, the energy of the surface wag modes is confined to just a few Si-H atoms. This energy propagates by resonant coupling on the surface much faster than it can decay into bulk modes. This holds until the surface reaches thermal equilibrium, and then the surface wag modes decay into bulk modes and the entire nanowire reaches thermal equilibrium. The implication is that the surface does reduce the thermal conductivity, but not by scattering bulk phonons. Instead, one must wait for part of the heat to propagate through the bulk and part along the surface before thermal equilibrium is reached.

A single fit to $T(t)$ in the central slice of the various nanowires leads to the following thermal conductivities $\kappa(T = 125\text{ K})$, in W/mK: 0.21 for $\text{Si}_{200}(\text{OH})_{32}$, 0.22 for $\text{Si}_{200}\text{H}_{32}$; 0.27 for $\text{Si}_{200}\text{D}_{32}$; 0.14 for $\text{Si}_{296}\text{H}_{112}$; and 0.16 for $\text{Si}_{296}\text{D}_{112}$. A larger number of surface atoms reduces the thermal conductivity as the amount of heat carried by surface atoms increases. The H, D isotope effect we obtain is associated with the change of frequency of the wag mode. Replacing H by the heavier D leads to lower-frequency surface wag modes, faster resonant coupling between adjacent modes on the surface, and an increase in the thermal conductivity relative to the corresponding H-saturated nanowire.

The (OH)-terminated nanowire is a poor representation of the surface oxide layer normally found on Si nanowires in a laboratory setting. Indeed, the H atoms at the end of the long Si–O–H surface bonds oscillate in vacuum with a very large amplitudes. Such a termination is unlikely to survive at room temperature.

B. δ layers, phonon trapping, and decay of vibrational excitations

We also investigated the role of impurities, in particular that of a monoatomic δ layer of C (lighter than Si) or Ge (heavier than Si). Such δ layers can, in principle, be incorporated during the growth of a nanowire more easily than a random distribution of impurities. We prepare the supercell in thermal equilibrium at 115 K and setup a temperature gradient by preparing a thin slice at the left end of the supercell at 270 K (the final equilibrium temperature is 125 K).

Since our supercells are periodic along the x direction, there is an image hot slice just beyond the end of the nanowire and

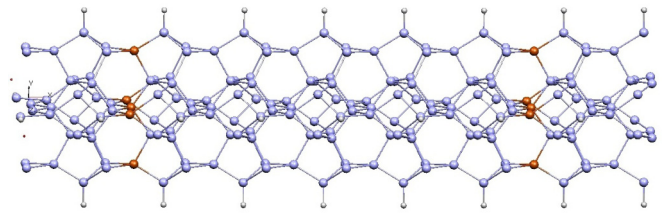


FIG. 12. (Color online) The $\text{Si}_{190}\text{X}_{10}\text{H}_{32}$ supercell with a monoatomic δ layer ($X = \text{C}$ or Ge) on either side of the central slice where the temperature is recorded.

the change in temperature in the central slice is caused by heat coming from these two hot slices. For this reason, we incorporated two monoatomic C or Ge δ layers, as shown in Fig. 12.

The monoatomic layers discussed here constitute a defect that covers the entire cross-sectional area of the nanowire. The SLMs associated with this defect are associated with the Si-C or Si-Ge bonds. The localization of these SLMs is shown in Fig. 13. In the case of the Ge δ layer, there are a number of SLMs below 100 cm^{-1} , while in the case of C, the highly localized SLMs are all above 550 cm^{-1} and are therefore much less likely to be populated. In both cases, however, there are numerous more weakly localized modes with low frequencies, corresponding the bending and twisting modes.

The propagating bulk phonons interact with the δ layer by displacing the Ge (or C) atoms, thus exciting some SLMs. Phonons trap at the defect. The trapped phonons then decay into bulk phonons of lower frequency. Since there are equivalent Si atoms on both sides of the δ layer, the probability of decay on either side would be the same were it not for the presence of the temperature gradient. Thus a monoatomic δ layer of Ge or C reduces the thermal conductivity by comparable amounts, the difference being due to slight differences in the lifetimes of the vibrational excitation in the SLMs associated with Ge or C. Such low-frequency modes have more than one decay channel. We calculated [14] these lifetimes for a C-related SLM at 556 cm^{-1} (10.5 and 17.2 ps) and a Ge-related SLM at 426 cm^{-1} (3.5 and

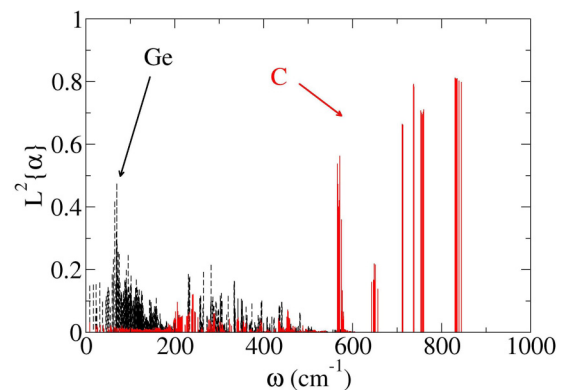


FIG. 13. (Color online) Spatial localization $L^2\{\alpha\}$ of the modes associated with (solid red lines) or Ge (dashed black lines) δ layer in $\text{Si}_{190}\text{X}_{10}\text{H}_{32}$ ($X = \text{C}$ or Ge).

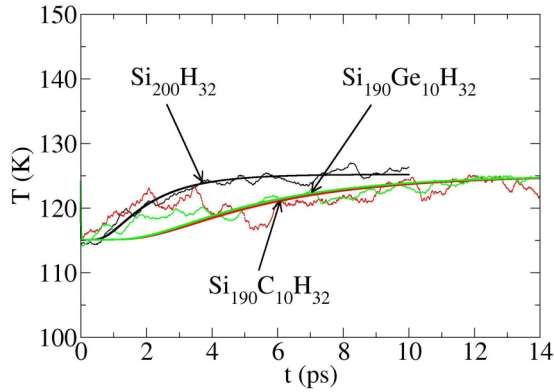


FIG. 14. (Color online) Temperature vs time in the central slice of the perfect $\text{Si}_{200}\text{H}_{32}$ supercell compared to that in the presence of two monoatomic δ layers of Ge or C atoms.

6.8 ps). For comparison bulk modes at 424 and 241 cm^{-1} have vibrational lifetimes in the range 0.2 to 0.8 ps.

The temperature versus time for the perfect and delta-doped nanowires are compared in Fig. 14. A thin slice on the left end of the $\text{Si}_{200}\text{H}_{32}$ supercell was prepared at 270 K and the rest of the supercell at 115 K . After reaching thermal equilibrium, the final temperature of the central slices has increased from 115 to 125 K . The calculated thermal conductivities are 0.22 (perfect nanowire), 0.09 (with a Ge δ layer), and 0.07 W/mK (with a C δ layer).

Note that the monoatomic δ layers considered here are qualitatively different from those containing several layers of C or Ge atoms). In the latter case, one deals with a Si-like phonon density of states on one side of the interface and a Ge- (or C-like) one on the other. The decay of the phonons trapped in the interface SLMs involves very different receiving modes on the two sides of the interface, leading to different coefficients of reflection and transmission. This situation will be discussed elsewhere [43].

The monoatomic δ layer is more efficient at reducing the thermal conductivity than randomly distributed Ge or C impurities in the nanowire. We have performed calculations in $\text{Si}_{188}\text{X}_{12}\text{H}_{32}$ with $\text{X} = \text{Ge}$ (or C), and obtained $\kappa(T = 125\text{ K}) = 0.16$ (with twelve Ge substitutional impurities) and 0.17 W/mK (with twelve C substitutional impurities).

IV. KEY POINTS AND DISCUSSION

We used the theoretical laser-flash technique to calculate the impact of defects on the thermal conductivity of Si nanowires. The method involves density-functional theory

for the electronic states. The eigenvectors of the dynamical matrix are used to prepare the nanowire slightly away from equilibrium and then *ab initio* MD simulations are performed (without thermostat) to monitor how the system returns to equilibrium. The time dependence of the temperature in the central cell, averaged over many initial random distributions of mode phases and energies, is fitted to an analytic solution of the heat diffusion equation. The fit determines the thermal diffusivity, from which the thermal conductivity is obtained at the desired temperature. The calculated temperature dependence of the thermal conductivity as well as its dependence on the diameter of the nanowire compare well with the measured values extrapolated to the size of our nanowires.

The surface of the NW is saturated with H, D, or OH groups. The surface (wag) modes excited in the hot region of the nanowire do not couple to Si modes in the bulk and do not decay into bulk modes. Instead, as long as the surface is away from thermal equilibrium, the surface modes propagate by resonant coupling along the surface, independently of the Si-related modes in the bulk. Thermal equilibrium in the central slice is achieved only after the (faster) contribution of the bulk and the (slower) contribution of surface modes arrive.

A monoatomic δ layer of Ge or C across the nanowire reduces the thermal conductivity more efficiently than a random distribution of Ge or C impurities in the nanowire. The heat flow generated by the hot slice propagates along the nanowire. When it reaches the δ layer, some of the SLMs associated with it trap phonons for lengths of time of the order of 10 ps (typical of a two-phonon decay [41]). Such vibrational lifetimes are much longer than those of bulk modes. The trapped phonons ultimately decay into lower-frequency modes on either side of the δ layer. It is phonon trapping that reduces the thermal conductivity.

These and earlier calculations [14] show that the empirical concept of defects being static scattering centers for (bulk) phonons is incomplete. In situations where the concentration of defects is large (or locally large), the description of bulk phonon-defect interactions should include the dynamic properties of defects, in particular the SLMs associated with them.

ACKNOWLEDGMENTS

The authors are most thankful to T. M. Gibbons for sharing preliminary results of his calculations of vibrational lifetimes and decay channels of the surface Si-H wag modes. SKE's research is supported in part by the grant D-1126 from the R. A. Welch Foundation. Texas Tech's High Performance Computing Center has provided generous amounts of CPU time.

[1] R. Peierls, *Ann. Phys.* **3**, 1055 (1929).

[2] P. Carruthers, *Rev. Mod. Phys.* **33**, 92 (1961).

[3] P. G. Klemens, *Proc. Phys. Soc. A* **68**, 1113 (1955); P. G. Klemens, *Solid State Physics: Advances and Applications*, edited by F. Seitz and D. Turnbull (Academic, New York, 1988), Vol. 7.

[4] J. M. Ziman, *Electrons and Phonons* (Clarendon, Oxford, 1960), pp. 220–223.

[5] J. Callaway, *Phys. Rev.* **113**, 1046 (1959).

[6] D. A. Broido, M. Malorny, G. Birner, N. Mingo, and D. A. Stewart, *Appl. Phys. Lett.* **91**, 231922 (2007).

[7] Z. Wang and N. Mingo, *Appl. Phys. Lett.* **97**, 101903 (2010).

- [8] M. Kazan, G. Guisbiers, S. Pereira, M. R. Correia, P. Masri, A. Bruyant, S. Volz, and P. Royer, *J. Appl. Phys.* **107**, 083503 (2010).
- [9] P. Martin, Z. Aksamija, E. Pop, and U. Ravaioli, *Phys. Rev. Lett.* **102**, 125503 (2009).
- [10] M. Maldovan, *J. Appl. Phys.* **111**, 024311 (2012).
- [11] S. J. Pearton, J. W. Corbett, and M. Stavola, *Hydrogen in Crystalline Semiconductors* (Springer, Berlin, 1991), Chap. 5.
- [12] M. Steger, A. Yang, T. Sekiguchi, K. Saeedi, M. L. W. Thewalt, M. O. Henry, K. Johnston, H. Riemann, N. V. Abrosimov, M. F. Churbanov, A. V. Gusev, A. K. Kaliteevskii, O. N. Godisov, P. Becker, and H.-J. Pohl, *J. Appl. Phys.* **110**, 081301 (2011).
- [13] S. K. Estreicher, D. West, J. Goss, S. Knack, and J. Weber, *Phys. Rev. Lett.* **90**, 035504 (2003).
- [14] S. K. Estreicher, T. M. Gibbons, By. Kang, and M. B. Bebek, *J. Appl. Phys.* **115**, 012012 (2014).
- [15] G. Davies first mentioned phonon trapping in this context during a lecture at the 25th International Conference on Defects in Semiconductors (St. Petersburg, Russia, July 2009).
- [16] D. West and S. K. Estreicher, *Phys. Rev. Lett.* **96**, 115504 (2006).
- [17] D. West and S. K. Estreicher, *Phys. Rev. B* **75**, 075206 (2007).
- [18] K. K. Kohli, G. Davies, N. Q. Vinh, D. West, S. K. Estreicher, T. Gregorkiewicz, I. Izeddin, and K.M. Itoh, *Phys. Rev. Lett.* **96**, 225503 (2006).
- [19] J. Zoe and A. Balandin, *J. Appl. Phys.* **89**, 2932 (2001).
- [20] N. Mingo, *Phys. Rev. B* **68**, 113308 (2003).
- [21] X. Lu and J. Chu, *J. Appl. Phys.* **100**, 014305 (2006).
- [22] I. Ponomareva, D. Srivastava, and M. Menon, *Nano Lett.* **7**, 1155 (2007).
- [23] S. Wang, X. Liang, X. Xu, and T. Ohara, *J. Appl. Phys.* **105**, 014316 (2009).
- [24] *Theory of Defects in Semiconductors*, edited by D. A. Drabold and S. K. Estreicher (Springer, Berlin, 2007).
- [25] T. M. Gibbons and S. K. Estreicher, *Phys. Rev. Lett.* **102**, 255502 (2009); **103**, 099904(E) (2009).
- [26] T. M. Gibbons, By. Kang, S. K. Estreicher, and C. Carbogno, *Phys. Rev. B* **84**, 035317 (2011).
- [27] N. Troullier and J. L. Martins, *Phys. Rev. B* **43**, 1993 (1991).
- [28] L. Kleinman and D. M. Bylander, *Phys. Rev. Lett.* **48**, 1425 (1982).
- [29] D. M. Ceperley and B. J. Alder, *Phys. Rev. Lett.* **45**, 566 (1980).
- [30] J. P. Perdew and A. Zunger, *Phys. Rev. B* **23**, 5048 (1981).
- [31] D. Sánchez-Portal, P. Ordejón, E. Artacho, and J. M. Soler, *Int. J. Quant. Chem.* **65**, 453 (1997).
- [32] E. Artacho, D. Sánchez-Portal, P. Ordejón, A. García, and J. M. Soler, *Phys. Status Solidi B* **215**, 809 (1999).
- [33] O. F. Sankey and D. J. Niklewski, *Phys. Rev. B* **40**, 3979 (1989).
- [34] O. F. Sankey, D. J. Niklewski, D. A. Drabold, and J. D. Dow, *Phys. Rev. B* **41**, 12750 (1990).
- [35] E. Anglada, J. M. Soler, J. Junquera, and E. Artacho, *Phys. Rev. B* **66**, 205101 (2002).
- [36] S. Garcia-Gil, A. Garcia, N. Lorente, and P. Ordejón, *Phys. Rev. B* **79**, 075441 (2009).
- [37] H. Hellmann, *Einführung in die Quantenchemie* (Franz Deuticke, Leipzig, 1937), p. 285.
- [38] R. P. Feynman, *Phys. Rev.* **56**, 340 (1939).
- [39] W. J. Parker, R. J. Jenkins, C. P. Butler, and G. L. Abbot, *J. Appl. Phys.* **32**, 1679 (1961).
- [40] D. Li, Y. Wu, P. Kim, L. Shi, P. Yang, and A. Majumdar, *Appl. Phys. Lett.* **83**, 2934 (2003).
- [41] B. Sun, G. A. Shi, S. V. S. Nageswara Rao, M. Stavola, N. H. Tolk, S. K. Dixit, L. C. Feldman, and G. Lupke, *Phys. Rev. Lett.* **96**, 035501 (2006).
- [42] T. M. Gibbons (private communication).
- [43] M. B. Bebek and S. K. Estreicher (unpublished).